

Complementary Local and Extended Views of Bonding in the ThCr_2Si_2 and CaAl_2Si_2 Structures*

CHONG ZHENG

Department of Chemistry, Stanford University, Stanford, California 94305

AND ROALD HOFFMANN

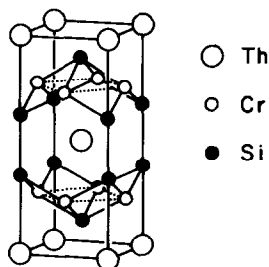
Department of Chemistry and Materials Science Center, Cornell University, Ithaca, New York 14853

Received January 15, 1987

Local and extended constructions of the bonding in transition metal AB_2X_2 compounds of ThCr_2Si_2 and CaAl_2Si_2 types are contrasted. From the local perspective, in the "inverted" XB_4 tetrahedral coordination observed in the CaAl_2Si_2 structure, the greater topological flexibility of the transition metal (B) d orbitals allow for better adjustment to the strain. Thus the difference between the strength of the 1-fold and the 3-fold $B-X$ bonds is small compared to the main group analogs. From the extended structure point of view, the metal sublattice in the CaAl_2Si_2 structure is less "dispersive" than in the ThCr_2Si_2 alternative. Hence, the metals interact better with the ligand sublattice at low ($\sim d^0$) and high ($\sim d^{10}$) electron counts. This may be one of the reasons the CaAl_2Si_2 structure occurs only for d^0 , d^5 , and d^{10} configurations at the transition metal. © 1988 Academic Press, Inc.

Introduction

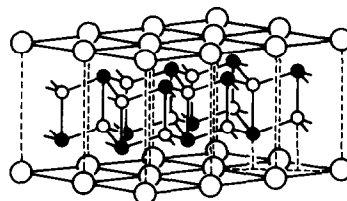
The ThCr_2Si_2 structure, **1**, accounts for more than 400 compounds of the AB_2X_2



1

composition (I). In these, A is typically a rare earth, an alkaline earth, or an alkali element, B is a transition metal or main group element, and X is an element of Group 15, 14, and occasionally 13.

Another prototype, CaAl_2Si_2 , **2**, is probably the runner-up in the structural popu-



○ Ca ○ Al ● Si

2

* Dedicated to John B. Goodenough with admiration for his insight into the electronic structure of extended materials.

larity competition in the AB_2X_2 series. Dozens of solids crystallize in the CaAl_2Si_2 mold (2). The apparent requirement that a legitimate AB_2X_2 candidate for the CaAl_2Si_2 AB_2X_2 structure have a d^0 , d^5 , or d^{10} configuration (2c) at atom B seems to limit the occurrence of this structural type. We should make the electron-counting scheme we use more precise. For example, if we take CaAl_2Si_2 (2a) and assign oxidation states as $\text{Ca}^{2+}(\text{Al}^{3+})_2(\text{Si}^{4-})_2$, we get a formal d^0 Al^{3+} , while $\text{Ca}^{2+}(\text{Mn}^{2+})_2(\text{P}^{3-})_2$ and $\text{Ca}^{2+}(\text{Zn}^{2+})_2(\text{P}^{3-})_2$ exemplify the d^5 and d^{10} cases. It should be mentioned that in general the fact that there is no short $X \cdots X$ contact in the CaAl_2Si_2 structure allows us to count Si and P as Si^{4-} and P^{3-} .

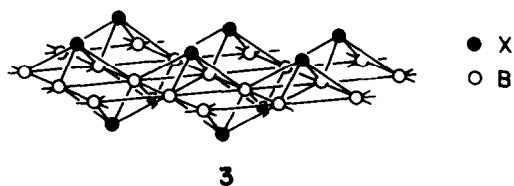
Thus, we are presented with this question: Why does a CaAl_2Si_2 -type compound have a d^0 , d^5 , or d^{10} configuration at the atom B ? And to approach an answer to this question we need to understand the structural details of both ThCr_2Si_2 and CaAl_2Si_2 structures. This we proceed to do with the assistance of calculations of the extended Hückel type. The computations do not take spin or magnetic interaction into account. But with the transparency of the method and our experience in this AB_2X_2 series (3), we hope to gain some insight into the nonmagnetic part of the forces that hold the solids together. The details of the calculations are given in the Appendix.

The ThCr_2Si_2 and CaAl_2Si_2 Structures

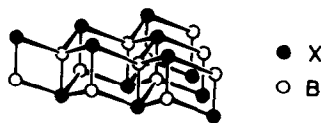
The ThCr_2Si_2 and CaAl_2Si_2 structures are shown in 1 and 2, respectively. Both stoichiometric AB_2X_2 compounds consist of interspersed $B_2X_2^{2-}$ layers and A^{n+} (mostly alkaline earth or rare earth) cation layers. The interactions between the cations and the anionic layers are predominantly ionic and should contribute very little to the electronic energy in which we are interested. That is why we will ignore the cations in our analysis and consider them

merely as electron donors, adding extra electrons into the host B_2X_2 layer. However, the ionic Madelung contribution is surely important in determining the stability of alternative structures. It could be superimposed on the electronic energy, and the reader is referred to our earlier qualitative analysis of this effect (3b).

The split B_2X_2 layers of the ThCr_2Si_2 and the CaAl_2Si_2 structures are shown in 3 and 4, respectively. The $B \cdots X$ contact is

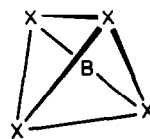


3



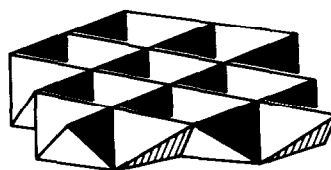
4

around 2.5 Å and the $X \cdots X$ one is very long, usually greater than 4 Å. Locally B resides at the center of an X_4 tetrahedron 5

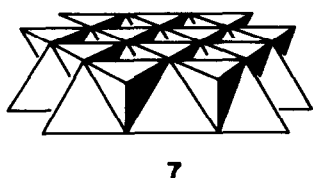


5

in both structures, and these tetrahedra pack differently to form the two types of crystals. In 6, each tetrahedron shares four of its six edges with others; in 7 it shares three.



6



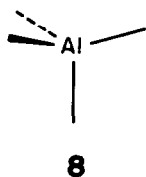
7

Given that the local environment of a B atom is the same tetrahedral one in both structures, it must be the extended, non-local interactions that favor one structure over the other. But before we explore the bonding from an extended point of view, let us look at the local bonding interactions in more detail.

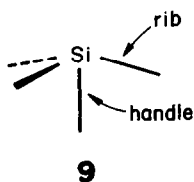
A Local View of Bonding

The d^0 and d^{10} configurations of B atoms in the CaAl_2Si_2 structure are relatively easy to rationalize in terms of the Zintl concept. An electron count of 0 or 10 for B in AB_2X_2 is coupled in our counting scheme with a full octet for X . We thus come to 8 or 18 electrons per BX (e.g., $[\text{Al}^{3+}\text{Si}^{4-}]^-$ in CaAl_2Si_2). This electron count is identical to that of C or ZnS, and so one might expect a similar three- or four-connected structure.

In fact, one does get a four-connected net in CaAl_2Si_2 , but it is not that of the diamond or wurtzite structure. The Al is at the center of a normal Si_4 tetrahedron, **8**; Si, however, is in an environment of an "inverted" Al_4 tetrahedron, **9**.



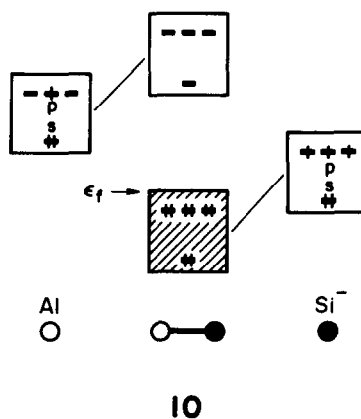
8



9

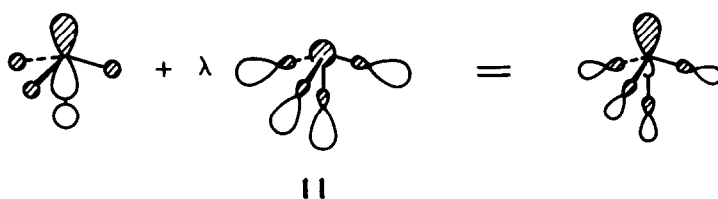
What about the the alternative ThCr_2Si_2 AB_2X_2 structure? The Cr, or B atom, is tetrahedrally surrounded by four X (and has also four close B neighbors). The X is also four-coordinate, but with the unusual square-pyramidal geometry. A special and fascinating feature of ThCr_2Si_2 structures is an interlayer $X-X$ contact that often becomes a bond. In most main group examples of this structure (e.g., BaAl_4 , REAl_2 Ga_2) this interlayer bond is present and strong. It makes X five-coordinate. Clearly, simple Zintl ideas do not apply. One needs to invoke and analyze the multi-center bonding that is present. We have done this in a previous contribution (3a) and have shown the similarity of the electron-deficient multi-center bonding in BaAl_4 to that in molecular B_5H_9 or $\text{B}_{10}\text{H}_{16}$. The appropriate electron count is 14 per B_2X_2 or 7 per BX . Putting 8 electrons per BX into this structure would fill some antibonding levels, so it is not surprising that the compounds under discussion in this paper prefer the four-connected Zintl structure of CaAl_2Zn_2 .

Let's examine in a little more detail the bonding in this structure. Schematically the bonding picture is that of **10**. Our previous



10

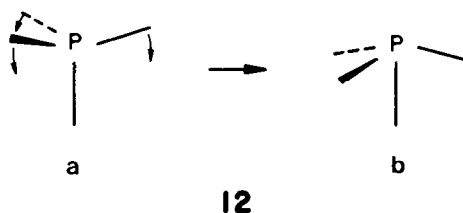
analysis (3c) shows that the HOMO of **10** can be described as a mixture of two orbitals derived from the LUMO and HOMO of



a perfect SiAl_4 tetrahedron. The mixing, **11**, weakens the vertical "handle" Si–Al bond, and in all the known d^0 and d^{10} CaAl_2Si_2 -type compounds that bond is longer than the "rib" Si–Al bond.

The d^5 compounds, however, seem to be different. Since they are going to be the main subject of our discussion, we list some of these compounds in Table I. In most of the d^5 Mn compounds in Table I, the difference in length between the "rib" and the "handle" bonds is small, and in some the "handle" bond is even shorter.

Let us study this geometrical distinction (or lack of it) in the d^5 structures with a model molecular PMn_4 cluster. We will begin with an ideal tetrahedron around P, and then deform it, **12**.

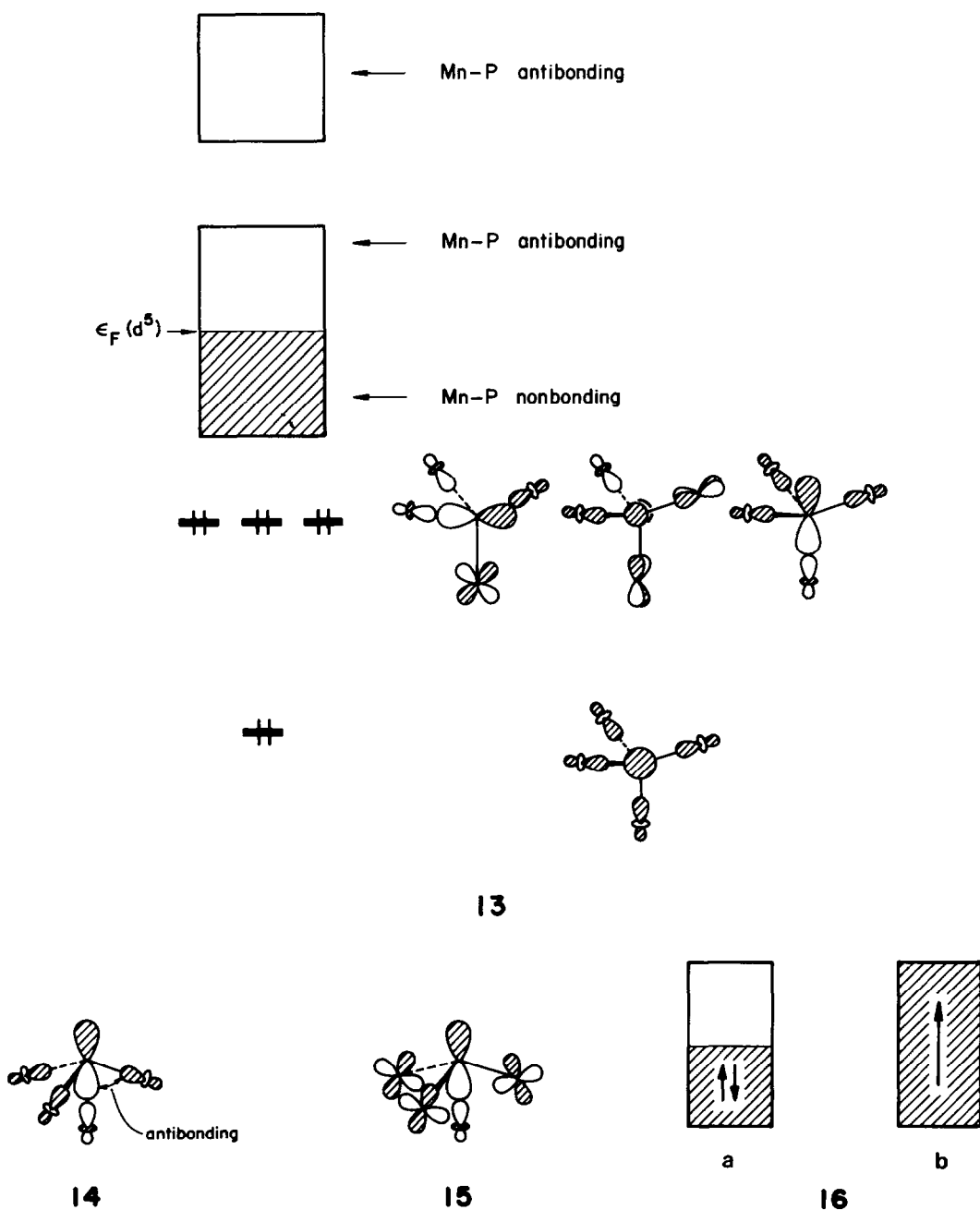


A schematic orbital diagram for the ideal PMn_4 tetrahedron is shown in **13**. The lowest four orbitals are mainly phosphorus s and p orbitals combined with symmetry-adapted Mn local radial σ orbitals ($d_{z^2} + s + p_z$). Above these four orbitals are the 20 Mn d -block orbitals. Their nature matches expectations. At the bottom of the d block, the orbitals have mainly local Mn δ and π character and thus are Mn–P nonbonding. At the top of the block, one finds part of the antibonding counterparts to the lowest four orbitals of the scheme (the ones which are Mn–P bonding, mostly on P). Actually, the

major part of Mn–P antibonding is in still higher orbitals, originating from Mn $4s$, $4p$.

Now imagine the flipping process, **12**. The s , p_x , and p_y orbitals of phosphorus retain their overlaps with metal orbitals and thus remain approximately the same in energy. But p_z , **14**, increases in energy because of antibonding between the p and rib Mn orbitals. This orbital actually rises to the top of the d block. Replacing it is another orbital, originally of local Mn π character, **15**, coming down from the d block. There are many Mn d orbitals at the same energy (as compared to only one s orbital at each Al in the main group CaAl_2Si_2 case) and thus more topological flexibility in PMn_4 compared to SiAl_4 . The bonding interactions in **15** can adjust better to the deformation; the rib bonds need not weaken so much.

In our extended Hückel calculations, we follow the bond strength by carrying out calculations on a model with symmetry-nonequivalent (here rib and handle) bonds set *equal* in length, and then we look at the *unequal* overlap populations that result as indicators of bonding changes that will take place. The Mn containing CaAl_2Si_2 phases present a special problem in that we do not know, experimentally, the spin state of Mn in them. Mn(II) is, of course, an ideal candidate for a high-spin magnetic solid. We think one must consider, therefore, two possible situations, drawn schematically in **16a** and **16b**. In **16a**, the low-spin case, the bottom of the d band is occupied by two electrons per orbital. In **16b**, the high-spin alternative, there is one electron per band. Our calculations unfortunately do not include spin explicitly, and so cannot deter-

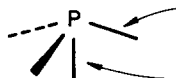
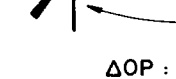


mine the energetics of these alternatives. In the remainder of the paper we will usually give the results for both alternative cases.

Returning to the PMn_4 model, if we begin

with d^0 , the d band empty, the overlap populations still indicate a stronger handle bond, but compared to the main group case (3c), the bond strength differential is substantially smaller. Filling of the d block up

to d^5 (low spin) does not change the differential much, since those states filled are mostly Mn–P nonbonding. If we choose instead the high-spin filling, one electron per band in the entire d band, then both axial and rib bonds are weakened. The orbitals at the top of the Mn d band are Mn–P antibonding. The actual overlap populations for low-spin and high-spin d^5 fillings, compared to those of the main group SiAl_4^{8+} cluster, are shown in 17. The

PMn_4^{5+}			
	low spin	high spin	SiAl_4^{8+}
	0.527	0.493	0.594
	0.371	0.361	0.362
ΔOP	0.156	0.132	0.232

17

difference between the rib and handle bond overlap populations is 0.156 (low spin) and 0.132 (high spin), compared to 0.232 in the main group case.

Let us go to the two-dimensional $\text{Mn}_2\text{P}_2^{2-}$ layer. In the infinite system, we have instead of a single energy level a bunch of states, or a density of states in the language of the trade. The overlap population equivalent is the COOP curve, shown in Fig. 1. The COOP curves are really overlap population-weighted densities of states and gauge the bonding capabilities of all the energy levels in a given energy interval (9). They are the solid state analog of an overlap population, with positive values indicating bonding, negative ones antibonding. Thus, the states around -20 and -15 eV, mostly phosphorus s and p , are Mn–P bonding. The states from -12 to -8 eV are the Mn d band. The lower half of the band is mainly Mn–P nonbonding and upper half antibonding. The handle Mn–P ($1\times$) bond is more antibonding in the upper part of the

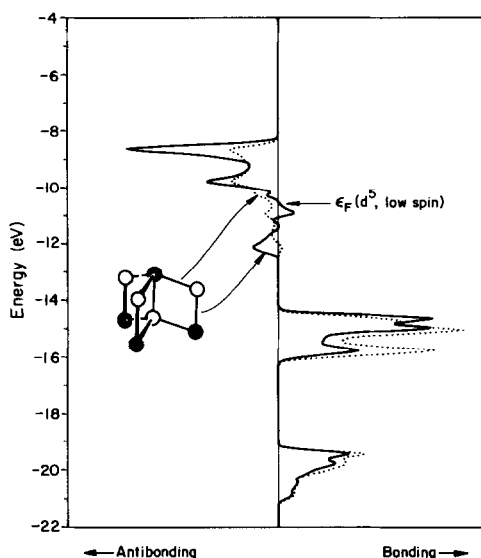

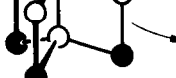


FIG. 1. Crystal orbital overlap population (COOP) curves for the two types of Mn–P bonds in $\text{Mn}_2\text{P}_2^{2-}$ (CaAl_2Si_2 type). The solid curve is for the 1-fold Mn–P bond and the dotted one for the 3-fold Mn–P bond.

d band. All of these features are expected from our discussion concerning 13, 14. The calculated overlap population for this infinite two-dimensional $\text{Mn}_2\text{P}_2^{2-}$ layer is shown in 18. As in the case of the PMn_4

$\text{Al}_2\text{Si}_2^{2-}$			
	low spin	high spin	$\text{Al}_2\text{Si}_2^{2-}$
	0.496	0.433	0.708
	0.386	0.287	0.460
ΔOP	0.110	0.146	0.248

18

cluster, the difference of 0.110 low spin and 0.146 high spin between the rib and handle bonds is substantially smaller than in the corresponding two-dimensional main group compound. Note that the high-spin occupation weakens the rib bond less than it does the handle bond, as expected from schematic 13.

Thus, we may conclude that for a d^5 compound of the CaAl_2Si_2 type, the bond length difference between the rib and

TABLE I
SOME d^5 CaAl_2Si_2 -TYPE COMPOUNDS

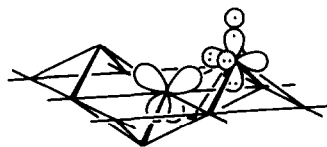
AB_2X_2 compound	Bond length (\AA)		Ref.
	Rib or $3 \times B-X$	Handle or $1 \times B-X$	
CaMn_2As_2	2.585	2.587	5
SrMn_2As_2	2.610	2.583	5
CaMn_2Sb_2	2.781	2.782	6
SrMn_2Sb_2	2.757	2.785	6
CaMn_2Bi_2	2.854	2.852	6
CaMn_2P_2	2.491	2.488	7
SrMn_2P_2	2.525	2.476	7
SrMn_2As_2	2.619	2.585	7
YbMnCuP_2	2.411	2.472	8

handle bonds is smaller, compared to a d^0 or d^{10} structure, as we have seen in Table I. This is consistent with the experimental observations.

The ThCr_2Si_2 Structure

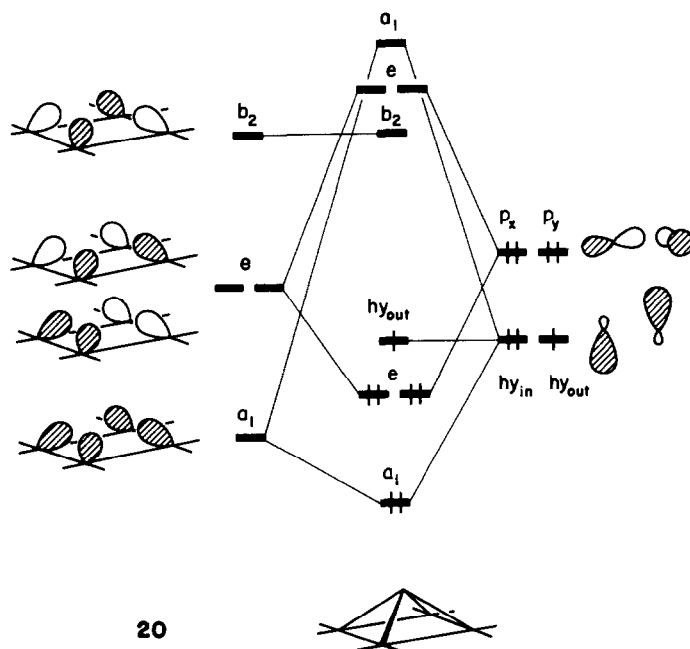
A bonding scheme for the ThCr_2Si_2 structure **3** can be constructed similarly by first

examining the local bonding and then turning on extended interactions. For the main group compounds (BaAl_4 , REAl_2Ga_2 , etc.) we have shown in a previous contribution (3a) that the bonding scheme is very similar to that of B_5H_9 or $\text{B}_{10}\text{H}_{16}$. Starting with a basis set of the sp^3 hybrids of the basal atom and the p_x , p_y , and sp hybrids of the apical atom, **19**, one forms cyclo-



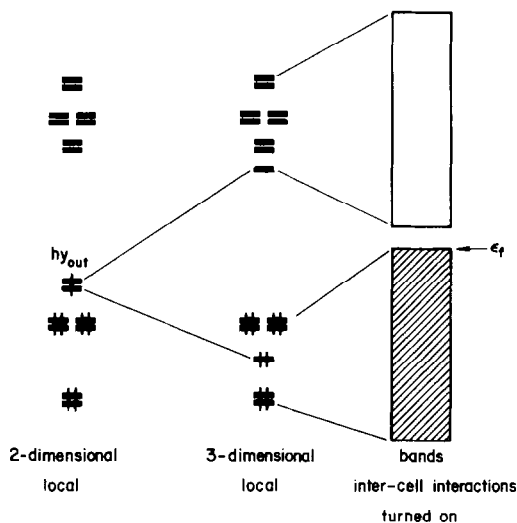
19

butadienoid symmetry-adapted linear combinations of the sp^3 orbitals to interact with the apical orbitals. This occurs at each hollow of the square lattice, **20**. The local bonding scheme, in which the apical hy_{in} , p_x , p_y interact with the basal a_1 and e MO's, respectively, produces three apical-basal bonding orbitals and one nonbonding one.



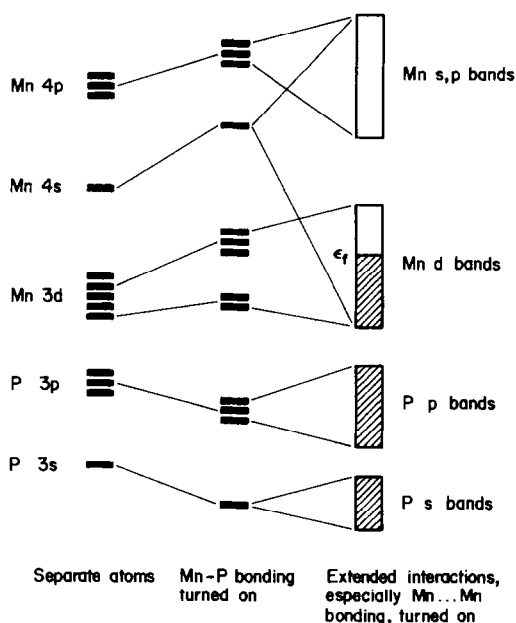
20

In three dimensions, two such hollow sites and the two $h_{y_{\text{out}}}$ orbitals from each form a bonding and an antibonding combination. This scheme accounts for the magic 14 electron per unit cell count in BaAl_4 -type compounds. Even after the delocalized interaction is turned on and each orbital develops into a band, the local character responsible for this electron count remains. The construction of the three-dimensional bands is shown schematically in 21.



21

For the transition metal case we can derive the approximate bands in a similar way. The local tetrahedral interaction splits the metal d orbitals into e and t sets, and when the extended interaction is turned on, both e and t sets develop into bands. This is shown schematically in 22. Thus we expect that the d band region is metal–ligand antibonding, more so at its top. The bottom of the d band should be metal–metal bonding and the top metal–metal antibonding. Our expectation is confirmed by the calculated COOP curves in Fig. 2, where the Mn–P antibonding and the Mn–Mn bonding/antibonding features between -12 and -9 eV are clearly seen.



22

Delocalized Construction

Let us approach the construction of the energy bands from another point of view. Imagine that the ligands (phosphorus, in our case) are stripped off from the layer lattice 3 and 4. The bare metal layers are then a square lattice, 23, and an AB closed-packed lattice, 24. In the square lattice,

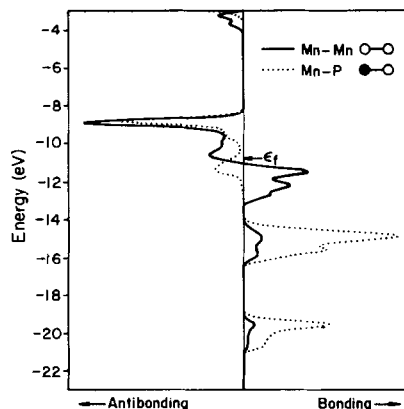
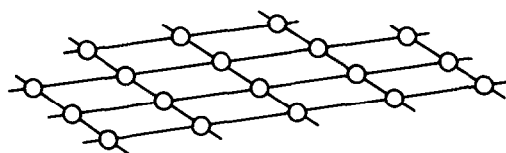
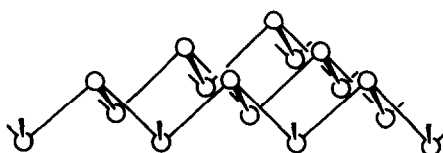


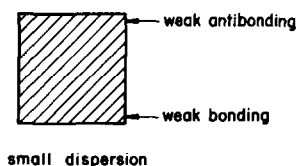
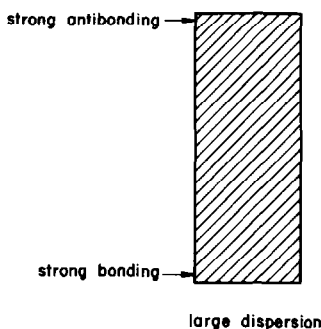
FIG. 2. COOP curves for the Mn–Mn (solid line) and Mn–P (dotted line) bonds in Mn_2P_2^- (ThCr_2Si_2 type).



23



24



25

each metal has four nearest neighbors and in the AB lattice, three. Thus for the same metal-metal distances (as assumed in our calculation), the d band dispersion is larger in **23** than in **24**. A band of greater dispersion has associated with it both strong bonding and antibonding at the bottom and top, respectively. And a little-dispersed band implies weaker nearest-neighbor interactions both bonding and antibonding. These situations are contrasted in **25**.

The energetic consequences of dispersion are a function of band filling. If the bands are completely filled, it might seem at first sight that there should be no energy difference between the two lattices. But this is not so. Just as in molecules (the corresponding phenomenon there is four-electron two-orbital repulsion), the antibonding at the top of the band is stronger than the bonding at the bottom. This is a consequence of including overlap in the calculations.

Following this line of reasoning, at low band filling, the lattice with larger band dispersion should be preferred, a conse-

quence of the strong bonding feature at the band bottom. But for high filling, the less dispersed band should be favored, avoiding the strong antibonding feature at the band top. Thus for our bare metal lattices, **23** and **24**, one would expect that the square lattice should be more stable at low d electron counts and the AB lattice at high d band filling.

The actual energetic difference computed between the two bare metal lattices from an extended Hückel calculation is shown in Fig. 3. At low d electron counts, indeed, the square lattice is favored, but at high band filling, it is again the square net which has lower energy. A detective decomposition of the M - M COOP curve (not shown here) tells us that this preference at the high electron filling is due to the metal s , p states, which penetrate into the top of the d band. Those states are of strong M - M bonding character for a more dispersive lattice. A picture, **26**, accounts for the shape of the curve in Fig. 3. In other words, higher dispersion is favored at high d electron counts, since the states populated

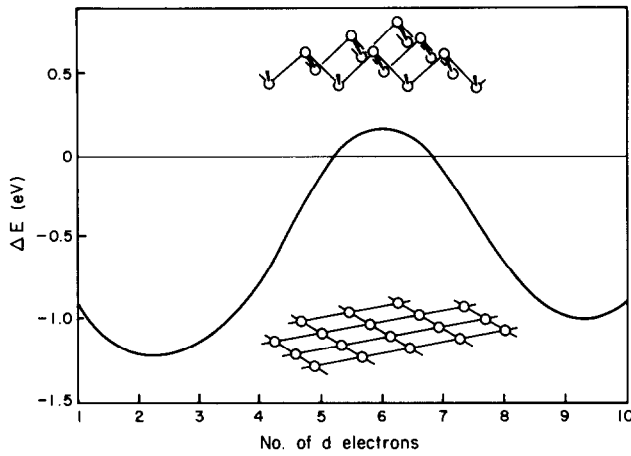
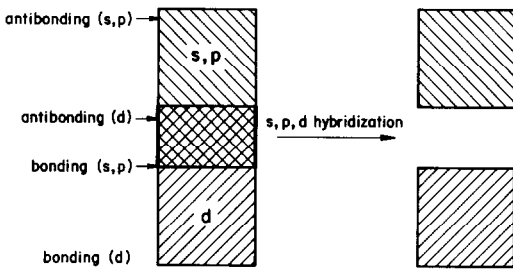


FIG. 3. Energy difference between the two metal sublattices of $\text{Mn}_2\text{P}_2^{2-}$ (CaAl_2Si_2 and ThCr_2Si_2 types). ΔE is defined as $E(\text{ThCr}_2\text{Si}_2) - E(\text{CaAl}_2\text{Si}_2)$; thus a positive ΔE means that the sublattice in the CaAl_2Si_2 type is more stable than that in the ThCr_2Si_2 type.

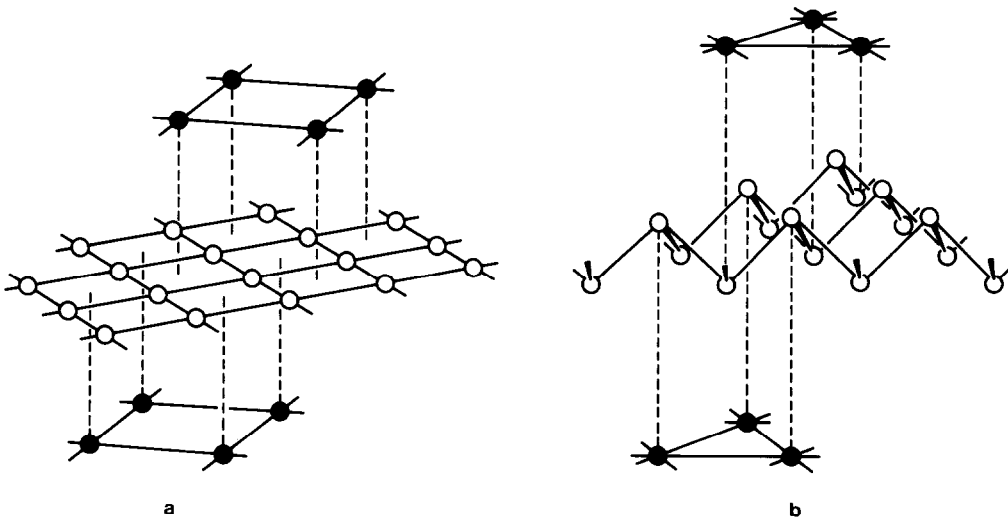


26

arose from the hybridization of the bottom of the s, p band with metal d .

Note that the shape of Fig. 3 corresponds to a typical fourth moment curve (10). A referee pointed out that it is smaller to the published curve of Burdett and Lee for α -bismuth and polonium (10) and could be interpreted in a similar way.

Now let us bring up to the metal sublattice the phosphorus sublattice, 27, and



27

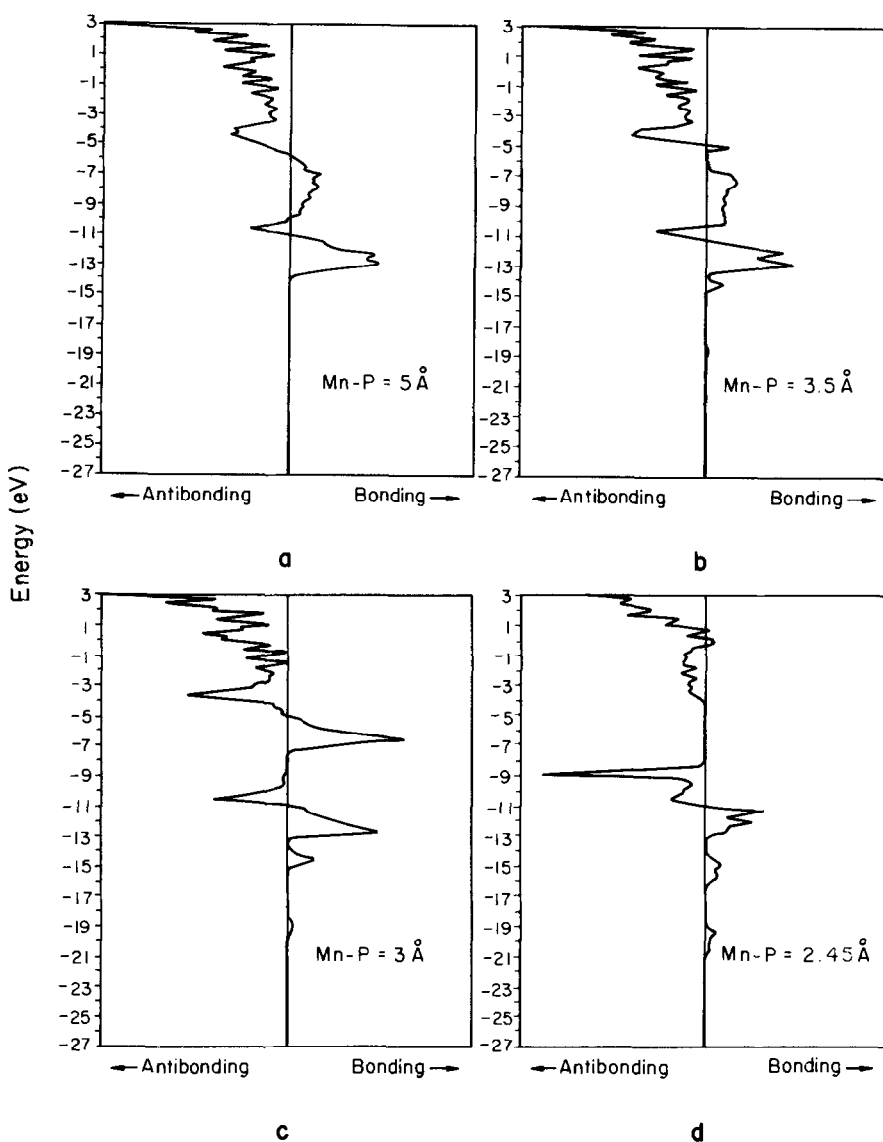


FIG. 4. COOP curves of the Mn-Mn bond in the ThCr_2Si_2 structure as that structure is assembled by bringing up the phosphorus sublattice to the transition metal sublattice. (a) $\text{Mn-P} = 5.0 \text{ \AA}$; (b) $\text{Mn-P} = 3.5 \text{ \AA}$; (c) $\text{Mn-P} = 3.0 \text{ \AA}$; (d) $\text{Mn-P} = 2.45 \text{ \AA}$ (ideal tetrahedral coordination).

follow the evolution of the bonding. Figure 4 shows the change of the COOP curve for the Mn-Mn bond in the ThCr_2Si_2 structure, **27a**, when we bring in the P sublattice from far ($\text{Mn-P} = 5 \text{ \AA}$) to the final ideal tetrahedron coordination ($\text{Mn-P} = 2.5 \text{ \AA}$). At a Mn-P separation of 5 \AA , there is no interac-

tion between the metal and ligand sublattices, and the COOP curve (Fig. 4a) is basically that of the bare square Mn lattice (**23**). At the bottom of the d band (-13 eV), it is Mn-Mn bonding. At the top (-10 eV) it is weakly antibonding, due to the mixing with the bottom of the s, p band (-8 eV).

At a closer Mn–P separation of 3.5 Å, the COOP (Fig. 4b) remains more or less the same, except that a small bump at -14 eV develops. This is a resonance with the phosphorus p band.

A Mn–P distance of 3 Å is within the interacting range, and we expect the COOP curve to change a lot. In Fig. 4c, we see that (1) a large portion of the states of Mn–Mn bonding character is pushed up, and (2) two resonant bumps at phosphorus s (~ -19 eV) and p (~ -14.5 eV) become more obvious. The states in these energy ranges are mainly P $3s$ and $3p$ and are primarily engaged in Mn–P bonding. But note that Mn–Mn bonding is picked up in these same bands.

We interpret the above observations as follows. Those metal states which are Mn–Mn bonding have, of course, fewer nodes in the metal sublattice than the Mn–Mn antibonding states. The approaching P ligands are coming down into the triangular or square hollows and there would sample effectively the presence or absence of nodes. Metal–P interaction is thus expected to be better for the metal states at the bottom of the metal band. These metal states divide after interaction into two parts: Mn–P bonding (resonating with phosphorus s and p levels) and Mn–P antibonding (pushed up). States which are strongly Mn–Mn antibonding interact less effectively with phosphorus and thus remain where they were at the energy scale. This is made clear by following the constant Mn–Mn d block antibonding feature in Fig. 4a \rightarrow 4d.

Figure 5 shows the metal–metal overlap population differences between the two crystal structures (overlap population of CaAl_2Si_2 minus that of ThCr_2Si_2). The solid curve is the Mn–Mn overlap population when the phosphorus sublattice is far away (5 Å). Since there is no Mn–P interaction, the curve should parallel, roughly, the energy curve for the bare lattices in Fig. 3.

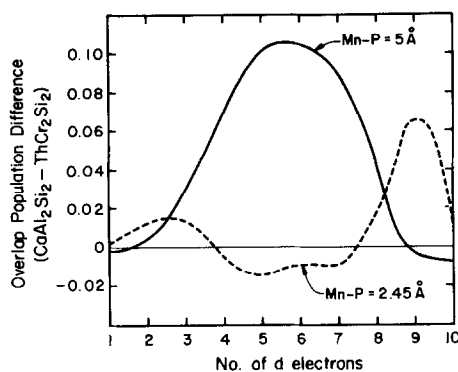


FIG. 5. Mn–Mn overlap population (OP) difference between the CaAl_2Si_2 - and ThCr_2Si_2 -type $\text{Mn}_2\text{P}_2^{2-}$ as the structures are assembled from metal and ligand sublattices. The difference is defined as $\text{OP}(\text{CaAl}_2\text{Si}_2) - \text{OP}(\text{ThCr}_2\text{Si}_2)$. Thus a positive value implies a stronger Mn–Mn bond in the CaAl_2Si_2 -type lattice.

In the ideal tetrahedral coordination (each phosphorus has four nearest metal neighbors in both structures), the overlap population difference (dashed curve) is “inverted.” The M – M bond becomes weaker in one lattice at the d electron count where it was stronger, and vice versa, when the M – P interaction is turned on. This provides additional evidence for our conclusion that metal states which are more bonding interact more strongly with ligand states and thus are pushed up (emptied). Since locally metal–ligand coordination is the same in both structures, we expect that the metal–metal interaction which determines the d band dispersion should be mainly responsible for the energetics. In our calculation, the overlap population indicates that the rib M – P bond in the CaAl_2Si_2 structure is always stronger and the handle bond weaker than the M – P bond in the ThCr_2Si_2 structure.

Figure 6 shows the energy difference between the two structures for two M – P separations (5 and 2.45 Å). A positive energy means the CaAl_2Si_2 structure is favored. These curves resemble those in Fig. 5. At electron counts close to d^0 or d^{10} ,

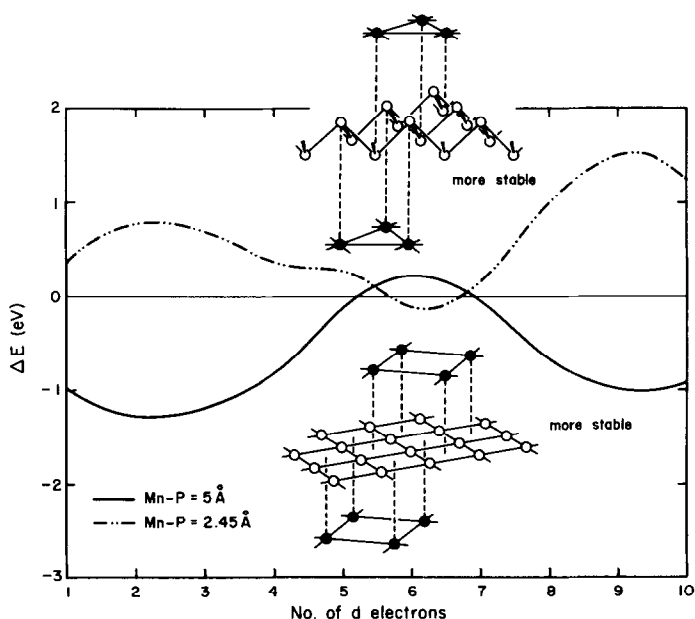


FIG. 6. Energy difference between the CaAl_2Si_2 - and ThCr_2Si_2 -type Mn_2P_2^- compounds as these are constructed by bringing up the phosphorus sublattice to the Mn sublattice. ΔE is defined as $E(\text{ThCr}_2\text{Si}_2) - E(\text{CaAl}_2\text{Si}_2)$. Thus a positive value means that the CaAl_2Si_2 structure is more stable than the ThCr_2Si_2 one.

the CaAl_2Si_2 structure is favored, partly due to the fact that fewer $M-M$ bonding states are pushed up by the $M-P$ interaction in the less dispersive metal sublattice in this structure. There is greater probability that an AB_2X_2 compound will fall into the CaAl_2Si_2 structure at a configuration d^0 or d^{10} . Interestingly, magnetic susceptibility measurements of YbZn_2P_2 and other compounds by Zwiener *et al.* (13) indicate that Yb has an intermediate valence between Yb^{2+} and Yb^{3+} . In this case, the host lattice B_2X_2 need not possess a d^{10} configuration.

Could we take the shape of the relative stability curve (Fig. 6) of the two structures as an indirect argument for the Mn compounds crystallizing in the CaAl_2Si_2 structure type as being high spin? Figure 6 is computed for a low-spin, paired electron assignment, and the region around d^5 is one

of maximum ThCr_2Si_2 structure stability. We do not have the energetics of electron repulsions and magnetic interaction in our calculations, so we cannot compare high-spin alternatives with any confidence. But roughly speaking, the electron distribution in a high-spin d^5 compound is going to resemble an average of d^0 and d^{10} , which would return us to a region of CaAl_2Si_2 structural stability.

We have so far explored the nonmagnetic interaction that determines the relative stabilities of the CaAl_2Si_2 and ThCr_2Si_2 structures. It would be interesting to investigate, experimentally, magnetic properties of these marvelous compounds, particularly the d^5 CaAl_2Si_2 type. Our understanding of the peculiar requirement of d^0 , d^5 , and d^{10} configurations in the CaAl_2Si_2 structure would be aided by such studies.

TABLE II
EXTENDED HÜCKEL PARAMETERS

Orbital	H_{ii} (eV)	ζ_1^a	ζ_2	c_1^a	c_2
Mn 3d	-11.67	5.15	1.7	0.5140	0.6930
4s	-9.75	1.8			
4p	-5.89	1.8			
P 3s	-18.6	1.8			
3p	-14.0	1.8			

^a Exponents and coefficients in a double ζ expansion of the 3d orbitals.

Appendix

The extended Hückel method (11) was used in all calculations. A rigid band model with fixed Mn and P parameters (listed in Table II) was chosen to represent the transition series. A Mn–Mn distance of 2.83 Å and M–P 2.45 Å was employed so that an ideal tetrahedral packing in both structures is realized. A 30 k -point set is used in the irreducible wedge in the Brillouin zone to calculate DOS and COOP and total energies according to Ref. (12).

Acknowledgments

This research was supported by the National Science Foundation through Grant CHE 84-06119 and DMR 821722 to the Material Science Center at Cornell University. We are grateful to Linda Kapitany for the typing and Jane Jorgensen and Elisabeth Fields for the drawings.

References

- (a) R. MARCHAND AND W. JEITSCHKO, *J. Solid State Chem.* **24**, 351 (1978); W. JEITSCHKO AND B. JABERG, *J. Solid State Chem.* **35**, 312 (1980); W. K. HOFMANN AND W. JEITSCHKO, *J. Solid State Chem.* **51**, 152 (1984). (b) E. PARTHÉ, B. CHABOT, H. F. BRAUN, AND N. ENGEL, *Acta Crystallogr. Sect. B* **39**, 588 (1983). (c) W. B. PEARSON, *J. Solid State Chem.* **56**, 278 (1985). (d) F. HULLIGER, *Helv. Phys. Acta* **53**, 216 (1985). (e) B. EISENMANN, N. MAY, W. MULLER, AND H. SCHÄFER, *Z. Naturforsch. B: Anorg. Chem., Org. Chem.* **27**, 1155 (1972).
- (a) E. I. GLADYSHEVSKII, P. I. KIPYAKEVICH, AND O. I. BODAK, *Ukr. Fiz. Zh. (Russ. Ed.)* **12**, 447 (1967). (b) K. DELLER AND B. EISENMANN, *Z. Naturforsch. B* **32**, 612 (1977). (c) P. KLÜFERS AND A. MEWIS, *Z. Naturforsch. B* **32**, 753 (1977). (d) A. MEWIS, *Z. Naturforsch. B* **33**, 382 (1978). (e) P. KLÜFERS, A. MEWIS, AND H.-U. SCHUSTER, *Z. Kristallogr.* **149**, 211 (1979). (f) E. BRECHTEL, G. CORDIER, AND H. SCHÄFER, *Z. Naturforsch. B* **34**, 921 (1979). (g) H.-U. SCHUSTER AND H.-O. FISCHER, *Z. Naturforsch. B* **34**, 1169 (1979). (h) A. MEWIS, *Z. Naturforsch. B* **35**, 939 (1980). (i) H.-O. FISCHER AND H.-U. SCHUSTER, *Z. Naturforsch. B* **35**, 1322 (1980). (j) A. MAHAN AND A. MEWIS, *Z. Naturforsch. B* **38**, 1041 (1983). (k) R. NESPER, H.-G. VON SCHNERING, AND J. CURDA, *Z. Naturforsch. B* **37**, 1514 (1982).
- (a) C. ZHENG AND R. HOFFMANN, *Z. Naturforsch. B* **41**, 292 (1986). (b) R. HOFFMANN AND C. ZHENG, *J. Phys. Chem.* **89**, 4175 (1985). (c) C. ZHENG, R. HOFFMANN, R. NESPER, AND H.-G. VON SCHNERING, *J. Amer. Chem. Soc.* **108**, 1876 (1986). (d) C. ZHENG AND R. HOFFMANN, *J. Amer. Chem. Soc.* **108**, 3078 (1986).
- See W. KLEMM, *Proc. Chem. Soc. London* **329** (1958); H. SCHÄFER, B. EISENMANN, AND W. MÜLLER, *Angew. Chem. Int. Ed. Engl.* **12**, 694 (1973).
- E. BRECHTEL, G. CORDIER, AND H. SCHÄFER, *Z. Naturforsch. B* **33**, 820 (1978).
- B. CORDIER AND H. SCHÄFER, *Z. Naturforsch. B* **31**, 1459 (1976).
- A. MEWIS, *Z. Naturforsch. B* **33**, 606 (1978).
- A. MEWIS, *Z. Naturforsch. B* **35**, 939 (1980).
- Some other applications of the COOP curves may be found in the following: (a) S. D. WIJESEKERA AND R. HOFFMANN, *Organometallics* **3**, 949 (1984). (b) M. KERTESZ AND R. HOFFMANN, *J. Amer. Chem. Soc.* **106**, 3453 (1984). (c) J.-Y. SAILLARD AND R. HOFFMANN, *J. Amer. Chem. Soc.* **106**, 2006 (1984).
- J. K. BURDETT AND S. LEE, *J. Amer. Chem. Soc.* **107**, 3050, 3063, 3083 (1985).
- R. HOFFMANN, *J. Chem. Phys.* **39**, 1397 (1963); R. HOFFMANN AND W. N. LIPSCOMB, *J. Chem. Phys.* **36**, 2179, 3489 (1962); *J. Chem. Phys.* **37**, 2872 (1962); J. H. AMMETER, H.-B. BÜRGI, J. C. THIBEAULT, AND R. HOFFMANN, *J. Amer. Chem. Soc.* **100**, 3686 (1978).
- J. D. PACK AND H. MONKHORST, *Phys. Rev. B* **16**, 1748 (1977).
- G. ZWIENER, M. NEUMANN, AND H.-U. SCHUSTER, *Z. Naturforsch. B* **36**, 1195 (1981).